

Environment-Driven Online LiDAR-Camera Extrinsic Calibration

Zhiwei Huang[✉], Graduate Student Member, IEEE, Jiaqi Li[✉], Student Member, IEEE,
 Ping Zhong[✉], Member, IEEE, Wei Ye[✉], Member, IEEE and Rui Fan[✉], Senior Member, IEEE

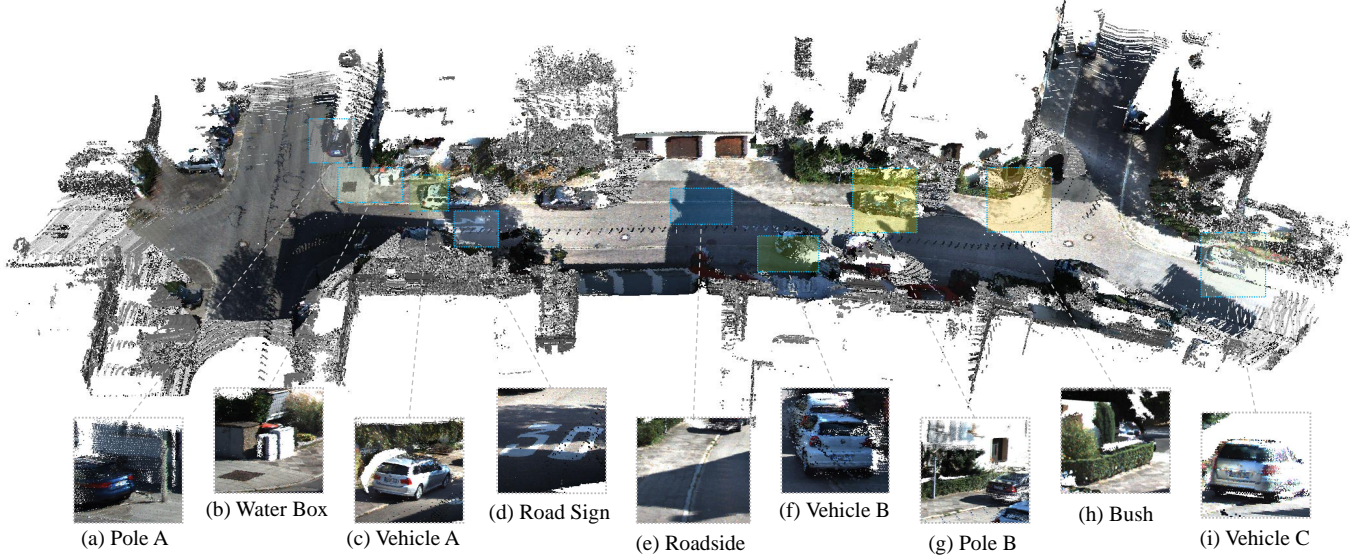


Fig. 1. Visualization of calibration results through LiDAR and camera data fusion in KITTI odometry 00 sequence: (a)-(i) zoomed-in regions that illustrate the alignment between the camera images and the LiDAR point clouds.

Abstract—LiDAR-camera extrinsic calibration (LCEC) is crucial for multi-modal data fusion in mechatronics. Existing methods, whether target-based or target-free, typically rely on customized calibration targets or fixed scene types, limiting their practicality in real-world applications. To address these challenges, we introduce EdO-LCEC, the first environment-driven online calibration approach. Unlike traditional target-free methods, EdO-LCEC observes the feature density of the application environment through a generalizable scene discrimi-

This research was supported by the National Natural Science Foundation of China under Grants 62473288 and 62233013, the Fundamental Research Funds for the Central Universities, Xiaomi Young Talents Program, and the National Key Laboratory of Human-Machine Hybrid Augmented Intelligence, Xi'an Jiaotong University under Grant No. HMHAI-202406. (*Corresponding author: Rui Fan*)

Zhiwei Huang, Jiaqi Li, and Wei Ye are with the Department of Control Science & Engineering, the College of Electronics & Information Engineering, Tongji University, Shanghai 201804, China (e-mails: {2431985, 2251550, yew}@tongji.edu.cn).

Ping Zhong is with the School of Computer Science and Engineering, Central South University, Changsha 410083, Hunan, China, as well as with the National Key Laboratory of Science and Technology on Automatic Target Recognition, National University of Defense Technology, Changsha 410073, Hunan, China (e-mail: ping.zhong@csu.edu.cn).

Rui Fan is with the Department of Control Science & Engineering, the College of Electronics & Information Engineering, Shanghai Research Institute for Intelligent Autonomous Systems, the State Key Laboratory of Intelligent Autonomous Systems, and Frontiers Science Center for Intelligent Autonomous Systems, Tongji University, Shanghai 201804, China, as well as with the National Key Laboratory of Human-Machine Hybrid Augmented Intelligence, Institute of Artificial Intelligence and Robotics, Xi'an Jiaotong University, Xi'an 710049, Shaanxi, China (e-mail: rui.fan@ieee.org).

nator. Based on this feature density, EdO-LCEC extracts LiDAR intensity and depth features from varying perspectives to achieve higher calibration accuracy. To overcome the challenges of cross-modal feature matching between LiDAR and camera, we propose dual-path correspondence matching (DPCM), which leverages both structural and textural consistency for reliable 3D-2D correspondences. Additionally, our approach models the calibration process as a joint optimization problem utilizing global constraints from multiple views and scenes to enhance accuracy. Extensive experiments on real-world datasets demonstrate that EdO-LCEC outperforms state-of-the-art methods, particularly in sparse or partially overlapping sensor views.

Index Terms—Environment-driven, LiDAR-camera extrinsic calibration, multi-modal data fusion.

I. INTRODUCTION

PERCEPTION is a critical challenge for autonomous mobile robots [1]. As the front-end module of mechatronic systems, it provides essential environmental information for high-level navigation. Modern LiDAR-camera fusion systems significantly enhance robotic perception capabilities [2]–[5]. While LiDARs provide accurate spatial information, cameras capture rich textural details [6]. Their complementary fusion enables robust performance in key robotic tasks including SLAM [7], [8] and object recognition [9]. LiDAR-camera extrinsic calibration (LCEC), which estimates the relative pose

between the two sensors, becomes a core and foundational process for effective data fusion in mechatronics.

Current LiDAR-camera extrinsic calibration methods are primarily categorized as either target-based or target-free. Target-based approaches [10]–[15] have long been the preferred choice in this field. They are typically offline, relying on customized calibration targets (typically checkerboards). However, they often demonstrate poor adaptability to real-world environments. This is largely because extrinsic parameters may change significantly due to moderate shocks or during extended operations in environments with vibrations. Online, target-free approaches aim at overcoming this problem by extracting informative visual features directly from the environment. Previous works [16], [17] estimate the extrinsic parameters by matching the cross-modal edges between LiDAR projections and camera images. While effective in specific scenarios with abundant features, these traditional methods heavily rely on well-distributed edge features. Recent advances in deep learning techniques have spurred extensive explorations, such as [18]–[20], to leverage semantic information to aid cross-modal feature matching. Although these approaches have shown compelling performance in specific scenarios, such as urban freeway, they predominantly rely on curated, pre-defined objects, *e.g.*, vehicles, lanes, and traffic poles. On the other hand, several end-to-end deep learning networks [21]–[26] have been developed to find a more direct solution for LCEC. While these methods have demonstrated effectiveness on their training datasets like KITTI [27], they highly rely on the training setup and are thus less generalizable. In our previous work, MIAS-LCEC [6], we developed a two-stage coarse-to-fine matching approach using the large vision model MobileSAM [28] to improve cross-modal feature matching. While this method achieves high accuracy with solid-state LiDARs (producing dense point clouds) when the sensors have overlapping fields of view, its performance significantly degrades in challenging scenarios with sparse or incomplete point clouds.

Although target-free LCEC methods eliminate the reliance on calibration targets, they struggle with complex, unstructured scenes due to their inability to adapt to environmental changes. To address this, we introduce environmental observation into target-free calibration, proposing the first environment-driven framework, EdO-LCEC. EdO-LCEC adapts to external conditions to maintain optimal performance by balancing the feature density between LiDAR projection and camera image. In this way, the system is no longer constrained by fixed strategies but can intelligently respond to environmental changes. Specifically, as illustrated in Fig. 1, we consider the working environment of the sensors as a sequence composed of multiple scenes. By selectively merging multiple scenes across different times, this approach could achieve high-precision calibration dynamically. A prerequisite for the success of EdO-LCEC is the design of a generalizable scene discriminator. The scene discriminator employs large vision models to conduct depth estimation and image segmentation. In detail, it calculates the feature density of the calibration scene and uses it to guide the generation of multiple virtual cameras for projecting LiDAR intensities and depth. This improved LiDAR point

cloud projecting strategy increases the available environmental features, and thus overcomes the previous reliance of algorithms [16], [29] on uniformly distributed geometric or textural features. At each scene, we perform dual-path correspondence matching (DPCM). Different from the C3M in MIAS-LCEC [6], DPCM divides correspondence matching into spatial and textural pathways to fully leverage both geometric and semantic information. Each pathway constructs a cost matrix based on structural and textural consistency, guided by accurate semantic priors, to yield reliable 3D-2D correspondences. Finally, the correspondences obtained from multiple views and scenes are used as inputs for our proposed multi-view and multi-scene joint optimization, which derives and refines the extrinsic matrix between LiDAR and camera. Through extensive experiments conducted on three real-world datasets, EdO-LCEC demonstrates superior robustness and accuracy compared to other SoTA approaches.

To summarize, our novel contributions are as follows:

- EdO-LCEC, the first environment-driven, online LCEC framework that introduces environmental observation into target-free calibration.
- Generalizable scene discriminator, which can automatically observe the calibration scene by evaluating the feature density through potential spatial, textural and semantic features extracted by SoTA LVMs.
- DPCM, a novel cross-modal feature matching algorithm consisting of textural and spatial pathways, capable of generating dense and reliable 3D-2D correspondences between LiDAR point cloud and camera image.
- Multi-view and multi-scene joint relative pose optimization, enabling high-quality extrinsic estimation by integrating multiple perspective views within a single scene and merging distinct scenes across different timestamps.

The remainder of this article is structured as follows: Sect. II reviews SoTA approaches in LCEC. Sect. III introduces EdO-LCEC, our proposed online, target-free LCEC algorithm. Sect. IV presents experimental results and compares our method with SoTA methods. Finally, in Sect. V, we conclude this article and discuss potential future research directions.

II. RELATED WORK

Target-based LCEC methods achieve high accuracy using customized calibration targets (typically checkerboards). However, they require offline execution and are significantly limited in dynamic or unstructured environments where such targets are unavailable [20], [30]. Recent studies have shifted to online, target-free approaches to overcome these limitations. Pioneering works [16], [17], [31]–[33] estimate the relative pose between the two sensors by aligning the cross-modal edges or mutual information (MI) extracted from LiDAR projections and camera RGB images. While effective in specific scenarios with abundant features, these traditional methods heavily rely on well-distributed edges and rich texture, which largely compromise calibration robustness. To circumvent the challenges associated with cross-modal feature matching, several studies [30], [34]–[36] have explored motion-based methods. These approaches match sensor motion trajectories from

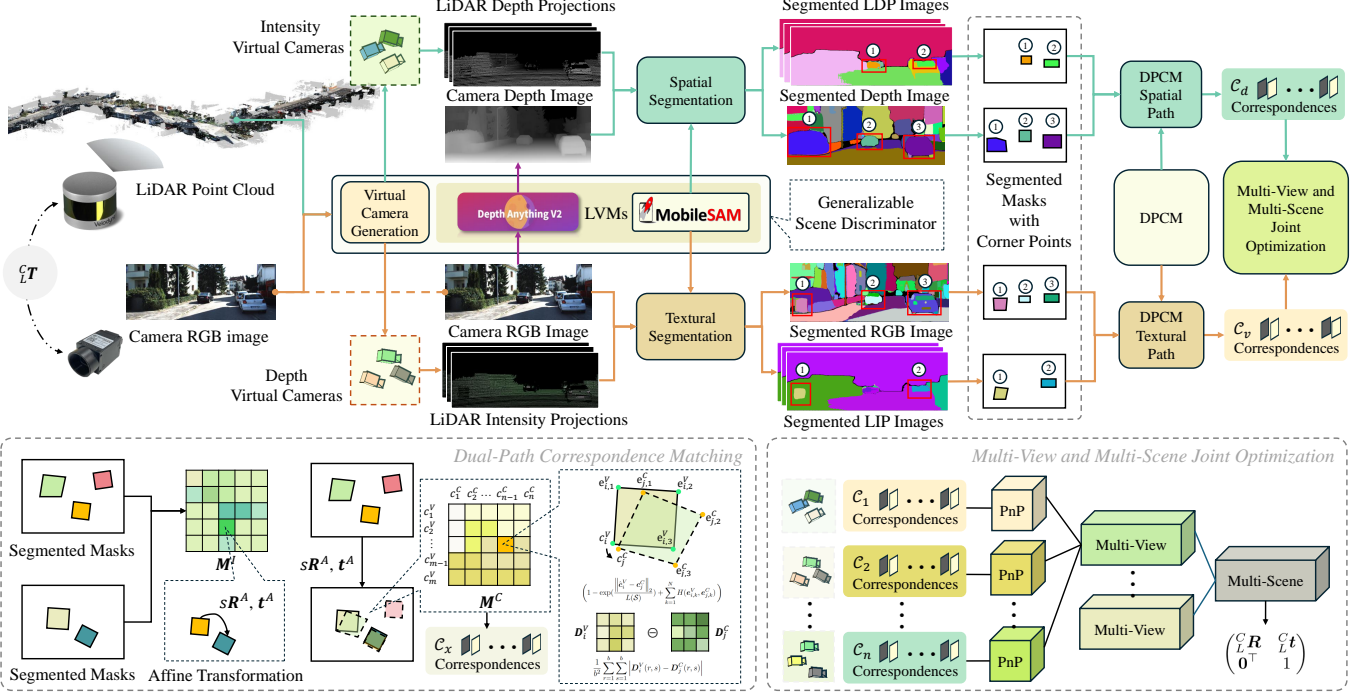


Fig. 2. The pipeline of our proposed EdO-LCEC. We use the generalizable scene discriminator to calculate the feature density of each calibration scene by image segmentation and depth estimation. Based on this feature density, the scene discriminator generates multiple depth and intensity virtual cameras to create LIP and LDP images. Image segmentation results (segmented masks with corner points) of virtual images and camera images are sent to the dual-path correspondence matching module to obtain dense 3D-2D correspondences, which serve as input for the multi-view and multi-scene joint optimization to derive and refine the extrinsic matrix between LiDAR and camera.

visual and LiDAR odometry to derive extrinsic parameters through optimization. While they effectively accommodate heterogeneous sensors without requiring overlap, they demand precise synchronized LiDAR point clouds and camera images to accurately estimate per-sensor motion, which limits their applicability in real-world scenarios.

Advances in deep learning techniques have driven significant exploration into enhancing traditional target-free algorithms. Some studies [6], [18]–[20], [29], [37]–[39] explore attaching deep learning modules to their calibration framework as useful tools to enhance calibration efficiency. For instance, [38] accomplishes LiDAR and camera registration by aligning road lanes and poles detected by semantic segmentation. Similarly, [19] employs stop signs as calibration primitives and refines results over time using a Kalman filter. A recent study [29] introduced Direct Visual LiDAR Calibration (DVL), a novel point-based method that utilizes SuperGlue [40] to establish direct 3D-2D correspondences between LiDAR and camera data. On the other hand, several learning-based algorithms [21]–[26] try to convert the calibration process into more direct approaches by exploiting end-to-end deep learning networks. Although these methods have demonstrated effectiveness on public datasets like KITTI [27], which primarily focuses on urban driving scenarios, their performance has not been extensively validated on other types of real-world datasets that contain more challenging scenes. Furthermore, their dependence on pre-defined sensor configurations (both LiDAR and camera) poses implementation challenges. In comparison, our approach introduces feature density evaluation to achieve

environmental observation. This environment-driven strategy enables robots to maintain high-precision calibration anytime and anywhere.

III. METHODOLOGY

Given LiDAR point clouds and camera images, our goal is to estimate their extrinsic matrix C_L^T , defined as follows:

$$C_L^T = \begin{bmatrix} C_L^R & C_L^t \\ \mathbf{0}^\top & 1 \end{bmatrix} \in SE(3), \quad (1)$$

where $C_L^R \in SO(3)$ represents the rotation matrix, C_L^t denotes the translation vector, and $\mathbf{0}$ represents a column vector of zeros. We first give an overview of the proposed method, as shown in Fig. 2. It mainly contains three stages:

- We first utilize a scene discriminator to perceive the environment through image segmentation and depth estimation, generating virtual cameras that project LiDAR intensity and depth from multiple viewpoints. LiDAR projections from multiple views are further segmented into masks with corner points (Sect. III-A).
- The segmented masks with detected corner points are processed along two pathways (spatial and textural) of the dual-path correspondence matching module to establish reliable 3D-2D correspondences (Sect. III-B).
- The obtained correspondences are used as inputs for our proposed multi-view and multi-scene joint optimization method, which derives and refines the extrinsic matrix C_L^T (Sect. III-C).

A. Generalizable Scene Discriminator

Our environment-driven approach first employs a generalizable scene discriminator to observe the surroundings by generating virtual cameras to project LiDAR point cloud intensities and depth. This discriminator configures both an intensity and a depth virtual camera from the LiDAR's perspective. This setup yields a LiDAR intensity projection (LIP) image ${}^V\mathbf{I} \in \mathbb{R}^{H \times W \times 1}$ (H and W represent the image height and width) and a LiDAR depth projection (LDP) image ${}^V\mathbf{D}$. To align with the LDP image, the input camera RGB image ${}^C\mathbf{I}$ is processed using Depth Anything V2 [41] to obtain estimated depth images ${}^C\mathbf{D}^1$. To take advantage of semantic information, we utilize MobileSAM [42] as the image segmentation backbone. The series of n detected masks in an image is defined as $\{\mathcal{M}_1, \dots, \mathcal{M}_n\}$. The corner points along the contours of masks detected are represented by $\{c_1, \dots, c_{m_i}\}$, where m_i is the total corner points number in the i -th mask. An instance (bounding box), utilized to precisely fit around each mask, is centrally positioned at \mathbf{o} and has a dimension of $h \times w$ pixels. To fully exploit the textural information, we evaluate the consistency of corner points using a texture matrix $\mathbf{D} \in \mathbb{R}^{b \times b}$, which encodes intensity values within a local $b \times b$ neighborhood. As depicted in Fig. 2, the neighboring vertices of a corner point c_i is defined as $\{e_{i,1}, \dots, e_{i,k}\}$. These neighboring vertices are used to calculate structural consistency in dual-path correspondence matching.

For each virtual or camera image \mathbf{I} , the scene discriminator computes its feature density $\rho(\mathbf{I})$, providing critical cues for feature extraction and correspondence matching. The feature density $\rho(\mathbf{I})$ is defined as follows:

$$\rho(\mathbf{I}) = \underbrace{\left(\frac{1}{n} \log \sum_{i=1}^n \frac{m_i}{|\mathcal{M}_i|} \right)}_{\rho_t} \underbrace{\left(\sum_{i=1}^n \log \frac{|\bigcap_{j=1}^n \mathcal{M}_j|}{|\mathcal{M}_i|} \right)}_{\rho_s}, \quad (2)$$

where ρ_t denotes the textural density and ρ_s represents the structural density. The occlusion challenges caused by the different perspectives of LiDAR and the camera [6], [16], combined with limited feature availability in sparse point clouds, mean that a single pair of virtual cameras is insufficient for a comprehensive view of the calibration scene. Let E represent the event of capturing enough effective features, with probability $P(E) = \lambda$. If we have n_I intensity virtual cameras and n_D depth virtual cameras, the probability of capturing enough effective features is $1 - (1 - \lambda)^{n_I + n_D}$. In theory, as $n_I + n_D \rightarrow \infty$, the probability $P(E')^{n_I + n_D} \rightarrow 0$, leading to $1 - (1 - \lambda)^{n_I + n_D} \rightarrow 1$. Increasing the number of virtual cameras raises the likelihood of capturing more potential correspondences, thus enhancing calibration accuracy. However, applying an infinite number of virtual cameras during calibration is impractical. Considering the trade-off between calibration accuracy and computational resources, we set the

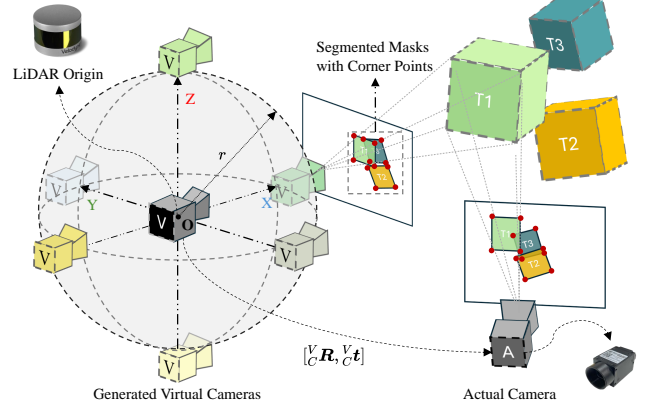


Fig. 3. Virtual camera generation method. We distribute virtual camera positions along the X , Y , and Z axes on a sphere of radius $r = 0.3$ m. The scene discriminator dynamically determines the number of virtual cameras based on feature density. All cameras maintain a default front-facing orientation.

number of multiple virtual cameras to satisfy the balance of feature density:

$$\rho({}^C\mathbf{I}) + \rho({}^D\mathbf{I}) = \sum_{i=0}^{n_I} \rho({}^V\mathbf{I}_i) + \sum_{i=0}^{n_D} \rho({}^V\mathbf{D}_i). \quad (3)$$

As depicted in Fig. 3, in practical applications, we set multiple virtual cameras inside a sphere originating from the LiDAR perspective center. Since the feature density is similar if the perspective viewpoints of virtual cameras are close to the initial position, we can assume that $\rho({}^V\mathbf{I}_i) \approx \rho({}^V\mathbf{I}_0)$ and $\rho({}^V\mathbf{D}_i) \approx \rho({}^V\mathbf{D}_0)$. So n_I and n_D can be obtained as follows:

$$n_I = \frac{\rho({}^C\mathbf{I})}{\rho({}^V\mathbf{I}_0)}, \quad n_D = \frac{\rho({}^D\mathbf{I})}{\rho({}^V\mathbf{D}_0)}. \quad (4)$$

Once all virtual cameras are generated, the discriminator performs image segmentation on each LiDAR projection captured from multiple views, detecting the corner points of the masks. These masks with detected corner points serve as inputs for the dual-path correspondence matching.

B. Dual-Path Correspondence Matching

Given the segmented masks with detected corner points, dual-path correspondence matching leverages them to achieve dense and reliable 3D-2D correspondences. DPCM consists of two pathways, one for correspondence matching of LIP and RGB images, and the other for LDP and depth images. For each pathway, DPCM adopted the approach outlined in [6] to obtain mask matching result $\mathcal{A} = \{(\mathcal{M}_i^V, \mathcal{M}_i^C) \mid i = 1, \dots, m\}$ from a cost matrix \mathbf{M}^I . Each matched mask pair can estimate an affine transformation $[s\mathbf{R}^A, \mathbf{t}^A] \in SE(2)$ to guide the correspondence matching. Specifically, we update the corner points c_i^V in the virtual image to a location \hat{c}_i^V that is close to its true projection coordinate using this affine transformation, as follows:

$$\hat{c}_i^V = s\mathbf{R}^A(c_i^V) + \mathbf{t}^A. \quad (5)$$

¹In this article, the symbols in the superscript denote the type of target camera (V denotes virtual camera and C indicates real camera), and the subscript denotes the source of the image (D is depth and I is intensity).

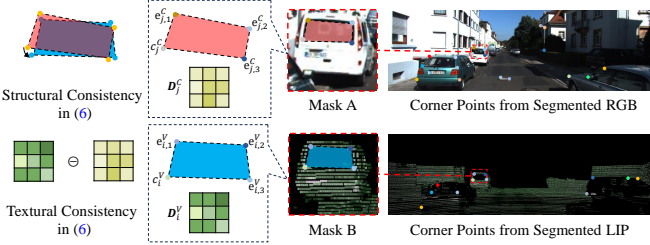


Fig. 4. DPCM utilizes structural consistency and textural consistency in (6) to compute matching cost between corner points detected from different segmented masks.

Algorithm 1 Dual-Path Correspondence Matching

Require:

Textural pathway: Segmented Masks (including detected corner points) obtained from the LIP and RGB image.

Spatial pathway: Segmented Masks (including detected corner points) obtained from the LDP and depth images.

Stage 1 (Reliable mask matching):

(1) Conduct cross-modal mask matching by adopting the method described in [6].

(2) Estimate sR^A and t^A using (9)-(12) in [6].

Stage 2 (Dense correspondence matching):

(1) For each pathway, update all masks in the virtual image using sR^A and t^A .

(2) Construct the corner point cost matrix M^C using (6).

(3) Select matches with the lowest costs in both horizontal and vertical directions of $M^C(x)$ as the optimum correspondence matches.

(4) Aggregate all corner point correspondences to form the sets $\mathcal{C} = \{(\mathbf{p}_i^L, \mathbf{p}_i) \mid i = 1, \dots, q\}$.

To determine optimum corner point matches, we construct a cost matrix M^C , where the element at $x = [i, j]^\top$, namely:

$$M^C(x) = \underbrace{\rho_s \left(1 - \exp\left(\frac{\|\hat{e}_i^V - \hat{e}_j^C\|^2}{L(\mathcal{A})}\right) + \sum_{k=1}^N H(e_{i,k}^V, e_{j,k}^C) \right)}_{\text{Structural Consistency}} + \underbrace{\rho_t \left(\frac{1}{b^2} \sum_{r=1}^b \sum_{s=1}^b \left| D_i^V(r, s) - D_j^C(r, s) \right| \right)}_{\text{Textural Consistency}} \quad (6)$$

denotes the matching cost between the i -th corner point of a mask in the LiDAR virtual image and the j -th corner point of a mask in the camera image. (6) consists of structural and textural consistency. As illustrated in Fig. 4, the structural consistency measures the structural difference of corner points in the virtual and real image, where $L(\mathcal{A})$ denotes the average perimeter of the matched masks and $H(e_{i,k}^V, e_{j,k}^C)$ represents the similarity of the neighboring vertices between current and target corner point. The textural consistency derives from the relative textural similarity of the b neighboring zone. After establishing the cost matrix, a strict criterion is applied to achieve reliable matching. Matches with the lowest costs

in both horizontal and vertical directions of $M^C(x)$ are determined as the optimum corner point matches. Since every \hat{e}_i^V can trace back to a LiDAR 3D point $\mathbf{p}_i^L = [x^L, y^L, z^L]^\top$, and every \hat{e}_i^C is related to a pixel $\mathbf{p}_i = [u, v]^\top$ (represented in homogeneous coordinates as $\tilde{\mathbf{p}}_i$) in the camera image, the final correspondence matching result of DPCM is $\mathcal{C} = \{(\mathbf{p}_i^L, \mathbf{p}_i) \mid i = 1, \dots, q\}$.

Leveraging the generalizable scene discriminator, the multi-perspective views generated by virtual cameras provide rich spatial-textural descriptors that effectively transform the feature matching problem into a robust 3D-2D correspondence establishment process. DPCM achieves efficient computation by verifying 2D structural and textural consistency instead of performing costly 3D point cloud registration. The pseudo-code of our DPCM is presented in Algorithm 1. During corner point matching within a mask, while the C3M in MIAS-LCEC exclusively considers points from the corresponding mask (*i.e.*, the matched mask associated with the current corner point), our DPCM in EdO-LCEC incorporates additional corner points from neighboring masks. This innovative matching strategy offers two key advantages: (1) it partially eliminates the dependency on dense, high-precision mask matching results, and (2) it substantially avoids errors induced by imperfect mask matching, especially under challenging conditions such as sparse LiDAR point clouds or limited LiDAR-camera FoV overlap.

C. Multi-View and Multi-Scene Joint Optimization

EdO-LCEC models the sensor's operational environment as a composition of N distinct scenes across different timestamps. While single-view methods (*e.g.*, [6], [16]) suffer from limited high-quality correspondences in sparse or incomplete point cloud scenarios, our environment-driven approach overcomes this constraint through integrating observations from multiple views and scenes. After establishing 3D-2D correspondences by DPCM, EdO-LCEC computes the extrinsic matrix between LiDAR and camera through a multi-view and multi-scene joint optimization. By aggregating optimal correspondences across time and space, our method enhances matching robustness, maximizes high-quality feature associations, and ultimately improves calibration accuracy.

In multi-view optimization, the extrinsic matrix ${}_L^C \hat{\mathbf{T}}_t$ of the t -th scene can be formulated as follows:

$${}_L^C \hat{\mathbf{T}}_t = \arg \min_{{}_L^C \mathbf{T}_{t,k}} \sum_{i=1}^{n+n_D} \sum_{(\mathbf{p}_j^L, \mathbf{p}_j) \in \mathcal{C}_i} G\left(\frac{\|\pi({}_L^C \mathbf{T}_{t,k} \mathbf{p}_j^L) - \tilde{\mathbf{p}}_j\|_2}{\epsilon_j}\right), \quad (7)$$

where ${}_L^C \mathbf{T}_{t,k}$ denotes the k -th PnP solution obtained using a selected subset \mathcal{V}_k of correspondences from \mathcal{C}_i , and ϵ_j represents the reprojection error of $(\mathbf{p}_i^L, \mathbf{p}_i)$ with respect to ${}_L^C \mathbf{T}_{t,k}$. $G(\epsilon_j)$ represents the gaussian depth-normalized reprojection error under the projection model π , defined as:

$$G(\epsilon_j) = \frac{\epsilon_j (e - \mathcal{K}(d'_j, \bar{d}'))}{H + \epsilon_j}, \quad (8)$$

where d'_j is the normalized depth of \mathbf{p}_j^L , \bar{d}' is the average normalized depth, and $\mathcal{K}(d'_j, \bar{d}')$ is a gaussian kernal.

In multi-scene optimization, we choose a reliable subset \mathcal{S}_t from each scenario, which can be obtained as follows:

$$\mathcal{S}_t = \bigcap_{k=1}^{s_t} \mathcal{V}_{t,k}, \quad s_t = \min \left\{ \frac{Q_{\max} q_t}{\sum_{j=1}^N q_j}, s_{\max} \right\}, \quad (9)$$

where $\mathcal{V}_{t,k}$ is the correspondence subset in the t -th scene with the k -th smallest mean reprojection error under its PnP solution. q_t denotes the number of correspondences in the t -th scene. Q_{\max} and s_{\max} represent the maximum number of subsets across all scenarios and the maximum number of reliable subsets in a single scene, respectively. The multi-scene optimization process then solves the final extrinsic matrix ${}^C_L \mathbf{T}^*$ by minimizing the joint reprojection error:

$$\mathcal{L}({}^C_L \mathbf{T}^*) = \sum_{t=1}^N \sum_{(\mathbf{p}_j^L, \mathbf{p}_j) \in \mathcal{S}_t} G \left(\left\| \pi({}^C_L \mathbf{T}^* \mathbf{p}_j^L) - \tilde{\mathbf{p}}_j \right\|_2 \right) \quad (10)$$

across multiple spaces in the environment at different times. This process combines optimal correspondences from both spatial and textural pathways in each scenario, enabling robust environment-driven optimization through multi-view and multi-scene fusion. As a result, our method achieves human-like adaptability to dynamic environments. This environment perception make EdO-LCEC behave much better than our previous method MIAS-LCEC, especially in conditions when point clouds are sparse or incomplete.

IV. EXPERIMENT

A. Experimental Setup and Evaluation Metrics

In our experiments, we compare our proposed EdO-LCEC with SoTA online, target-free LCEC approaches on the public dataset KITTI odometry [27] (including 00-09 sequences) and MIAS-LCEC [6] (including target-free datasets MIAS-LCEC-TF70 and MIAS-LCEC-TF360). To comprehensively evaluate the performance of LCEC approaches, we use the magnitude e_r of Euler angle error and the magnitude e_t^2 of the translation error, with the following expression:

$$\begin{aligned} e_r &= \left\| {}^C_L \mathbf{r}^* - {}^C_L \mathbf{r} \right\|_2, \\ e_t &= \left\| -({}^C_L \mathbf{R}^*)^{-1} {}^C_L \mathbf{t}^* + {}^C_L \mathbf{R}^{-1} {}^C_L \mathbf{t} \right\|_2, \end{aligned} \quad (11)$$

to quantify the calibration errors. In (11), ${}^C_L \mathbf{r}^*$ and ${}^C_L \mathbf{r}$ represent the estimated and ground-truth Euler angle vectors, computed from the rotation matrices ${}^C_L \mathbf{R}^*$ and ${}^C_L \mathbf{R}$, respectively. Similarly, ${}^C_L \mathbf{t}^*$ and ${}^C_L \mathbf{t}$ denote the estimated and ground-truth translation vectors from LiDAR to camera, respectively.

Notably, sequences in KITTI odometry, aside from 00, were included in the training datasets for the learning-based methods [22], [24], [26]. To ensure a fair comparison, we reproduced calibration results for both the left and right cameras on sequence 00 when the authors provided their code; otherwise, we used the reported results for the left camera from their papers. Since most learning-based methods lack APIs for custom data, our comparison with these methods is limited to the KITTI odometry 00 sequence. For experiments on the

²The translation from LiDAR pose to camera pose is $-{}^C_L \mathbf{R}^{-1} {}^C_L \mathbf{t}$ when (1) is used to depict the point translation.

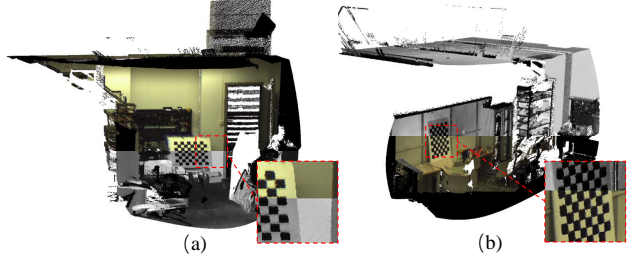


Fig. 5. Visualization of EdO-LCEC calibration results through LiDAR and camera data fusion: (a)-(b) illustrate two LiDAR point clouds in MIAS-LCEC-TF70, partially rendered by color using the estimated extrinsic matrix of EdO-LCEC.

MIAS-LCEC dataset, as the results for the compared methods [6], [16], [17], [29], [38] are reported in [6], we directly use the values presented in that paper.

Our algorithm was implemented on an Intel i7-14700K CPU and an NVIDIA RTX4070Ti Super GPU. The entire process of a single-view calibration, including scene discriminating, DPCM, and relative pose optimization, takes approximately 15 to 70 seconds.

B. Comparison with State-of-the-Art Method

In this section, quantitative comparisons with SoTA approaches on three datasets are presented in Fig. 8, Tables I³, II, III, and IV. Additionally, qualitative results are illustrated in Figs. 5 and 6.

1) *Evaluation on KITTI Odometry*: The results shown in Table I and II suggest that, with the exception of sequences 01 and 04, our method achieves SoTA performance across the ten sequences (00-09) in KITTI odometry. Specifically, in the 00 sequence, EdO-LCEC reduces the e_r by around 35.2-99.8% and the e_t by 11.8-98.7% for the left camera, and reduces the e_r by around 46.9-99.7% and the e_t by 13.9-97.6% for the right camera. Additionally, according to Fig. 6, it can be observed that the point cloud of a single frame in KITTI is so sparse that the other approaches behave poorly. In contrast, our proposed method overcomes this difficulty and achieves high-quality data fusion through the calibration result. We attribute these performance improvements to our multi-view and multi-scene joint optimization. Merging the optimal matching results from multiple views and scenes maximizes the number of reliable correspondences and ultimately improves overall calibration accuracy.

2) *Evaluation on MIAS-LCEC Dataset*: Compared to the sparse point clouds in KITTI odometry, the point clouds in the MIAS-LCEC datasets are significantly denser, which facilitates feature matching and allows us to test the upper limits of the algorithm calibration accuracy. The results shown in Table III demonstrate that our method outperforms all other SoTA approaches on MIAS-LCEC-TF70. It can also be observed that our method dramatically outperforms CRLF, UMich, DVL, HKU-Mars, and is slightly better than MIAS-LCEC across the total six subsets. In challenging conditions that are under poor illumination and adverse weather, or when

³The results generated by LCCNet using the authors' code yield higher errors compared to those reported in their paper.

TABLE I

QUANTITATIVE COMPARISONS WITH SOTA TARGET-FREE LCEC APPROACHES ON THE 00 SEQUENCE OF KITTI ODOMETRY. THE BEST RESULTS ARE SHOWN IN BOLD TYPE. \dagger : THESE METHODS DID NOT RELEASE CODE, PREVENTING THE REPRODUCTION OF RESULTS FOR BOTH CAMERAS.

Approach	Initial Range	Left Camera						Right Camera									
		Magnitude e_r ($^\circ$) e_t (m)		Rotation Error ($^\circ$) Yaw Pitch Roll			Translation Error (m) X Y Z			Magnitude e_r ($^\circ$) e_t (m)		Rotation Error ($^\circ$) Yaw Pitch Roll			Translation Error (m) X Y Z		
CalibRCNN \dagger [23]	$\pm 10^\circ / \pm 0.25m$	0.805	0.093	0.446	0.640	0.199	0.062	0.043	0.054	-	-	-	-	-	-	-	-
CalibDNN \dagger [24]	$\pm 10^\circ / \pm 0.25m$	1.021	0.115	0.200	0.990	0.150	0.055	0.032	0.096	-	-	-	-	-	-	-	-
RegNet \dagger [43]	$\pm 20^\circ / \pm 1.5m$	0.500	0.108	0.240	0.250	0.360	0.070	0.070	0.040	-	-	-	-	-	-	-	-
LCCNet [22]	$\pm 10^\circ / \pm 1.0m$	1.418	0.600	0.455	0.835	0.768	0.237	0.333	0.329	1.556	0.718	0.457	1.023	0.763	0.416	0.333	0.337
RGGNet [26]	$\pm 20^\circ / \pm 0.3m$	1.29	0.114	0.640	0.740	0.350	0.081	0.028	0.040	3.870	0.235	1.480	3.380	0.510	0.180	0.056	0.061
CalibNet [25]	$\pm 10^\circ / \pm 0.2m$	5.842	0.140	2.873	2.874	3.185	0.065	0.064	0.083	5.771	0.137	2.877	2.823	3.144	0.063	0.062	0.082
Borer <i>et al.</i> \dagger [21]	$\pm 1^\circ / \pm 0.25m$	0.455	0.095	0.100	0.440	0.060	0.037	0.030	0.082	-	-	-	-	-	-	-	-
CRLF [38]	-	0.629	4.118	0.033	0.464	0.416	3.648	1.483	0.550	0.633	4.606	0.039	0.458	0.424	4.055	1.636	0.644
UMich [17]	-	4.161	0.321	0.113	3.111	2.138	0.286	0.077	0.086	4.285	0.329	0.108	3.277	2.088	0.290	0.085	0.090
HKU-Mars [16]	-	33.84	6.355	19.89	18.71	19.32	3.353	3.232	2.419	32.89	4.913	18.99	15.77	17.00	2.917	2.564	1.646
DVL [29]	-	122.1	5.129	48.64	87.29	98.15	2.832	2.920	1.881	120.5	4.357	49.60	87.99	96.72	2.086	2.517	1.816
MIAS-LCEC [6]	-	5.385	1.014	1.574	4.029	4.338	0.724	0.383	0.343	7.655	1.342	1.910	5.666	6.154	0.843	0.730	0.358
EdO-LCEC (Ours)	-	0.295	0.082	0.117	0.176	0.150	0.051	0.044	0.032	0.336	0.118	0.216	0.168	0.121	0.083	0.067	0.032

TABLE II

COMPARISONS WITH SOTA LCEC APPROACHES ON KITTI ODOMETRY (01-09 SEQUENCES). THE BEST RESULTS ARE SHOWN IN BOLD TYPE.

Approach	01		02		03		04		05		06		07		08		09	
	e_r	e_t																
CRLF [38]	0.623	7.363	0.632	3.642	0.845	6.007	0.601	0.372	0.616	5.961	0.615	25.762	0.606	1.807	0.625	5.376	0.626	5.133
UMich [17]	2.196	0.305	3.733	0.331	3.201	0.316	2.086	0.348	3.526	0.356	2.914	0.353	3.928	0.368	3.722	0.367	3.117	0.363
HKU-Mars [16]	20.73	3.770	32.95	12.70	21.99	3.493	4.943	0.965	34.42	6.505	25.20	7.437	33.10	7.339	26.62	8.767	20.38	3.459
DVL [29]	112.0	2.514	120.6	4.285	124.7	4.711	113.5	4.871	123.9	4.286	128.9	5.408	124.7	5.279	126.2	4.461	116.7	3.931
MIAS-LCEC [6]	0.621	0.300	0.801	0.327	1.140	0.324	0.816	0.369	4.768	0.775	2.685	0.534	11.80	1.344	5.220	0.806	0.998	0.432
EdO-LCEC (Ours)	2.269	0.459	0.561	0.142	0.737	0.137	1.104	0.339	0.280	0.093	0.485	0.124	0.188	0.076	0.352	0.115	0.386	0.120

TABLE III

COMPARISONS WITH SOTA TARGET-FREE LCEC APPROACHES ON MIAS-LCEC-TF70. THE BEST RESULTS ARE SHOWN IN BOLD TYPE.

Approach	Residential Community		Urban Freeway		Building		Challenging Weather		Indoor		Challenging Illumination		All	
	e_r ($^\circ$)	e_t (m)	e_r ($^\circ$)	e_t (m)	e_r ($^\circ$)	e_t (m)	e_r ($^\circ$)	e_t (m)	e_r ($^\circ$)	e_t (m)	e_r ($^\circ$)	e_t (m)	e_r ($^\circ$)	e_t (m)
CRLF [38]	1.594	0.464	1.582	0.140	1.499	20.17	1.646	2.055	1.886	30.05	1.876	19.05	1.683	11.13
UMich [17]	4.829	0.387	2.267	0.166	11.914	0.781	1.851	0.310	2.029	0.109	5.012	0.330	4.265	0.333
HKU-Mars [16]	2.695	1.208	2.399	1.956	1.814	0.706	2.578	1.086	2.527	0.246	14.996	3.386	3.941	1.261
DVL [29]	0.193	0.063	0.298	0.124	0.200	0.087	0.181	0.052	0.391	0.030	1.747	0.377	0.423	0.100
MIAS-LCEC [6]	0.190	0.050	0.291	0.111	0.198	0.072	0.177	0.046	0.363	0.024	0.749	0.118	0.298	0.061
EdO-LCEC (Ours)	0.168	0.044	0.293	0.105	0.184	0.057	0.183	0.044	0.338	0.027	0.474	0.104	0.255	0.055

few geometric features are detectable, EdO-LCEC performs significantly better than all methods, particularly. This impressive performance can be attributed to the generalizable scene discriminator. The multiple virtual cameras generated by the scene discriminator provide a comprehensive perception of the calibration scene from both spatial and textural perspectives, which largely increases the possibility of capturing high-quality correspondences for the PnP solver. Furthermore, the data fusion results in Fig. 5, obtained using our optimized extrinsic matrix, visually demonstrate perfect alignment on the checkerboard. This highlights the high calibration accuracy achieved by our method.

Additionally, experimental results on the MIAS-LCEC-TF360 further prove our outstanding performance. From Table IV, it is evident that while the other approaches achieve poor performances, our method demonstrates excellent accuracy,

TABLE IV

QUANTITATIVE COMPARISONS OF OUR PROPOSED EdO-LCEC APPROACH WITH OTHER SOTA TARGET-FREE APPROACHES ON THE MIAS-LCEC-TF360. THE BEST RESULTS ARE SHOWN IN BOLD TYPE.

Approach	Indoor		Outdoor	
	e_r ($^\circ$)	e_t (m)	e_r ($^\circ$)	e_t (m)
CRLF [38]	1.479	13.241	1.442	0.139
UMich [17]	1.510	0.221	6.522	0.269
HKU-Mars [16]	85.834	7.342	35.383	8.542
DVL [29]	39.474	0.933	65.571	1.605
MIAS-LCEC [6]	0.996	0.182	0.659	0.114
EdO-LCEC (Ours)	0.720	0.106	0.349	0.109

indicating strong adaptability to more challenging scenarios, with narrow overlapping areas between LiDAR projections and

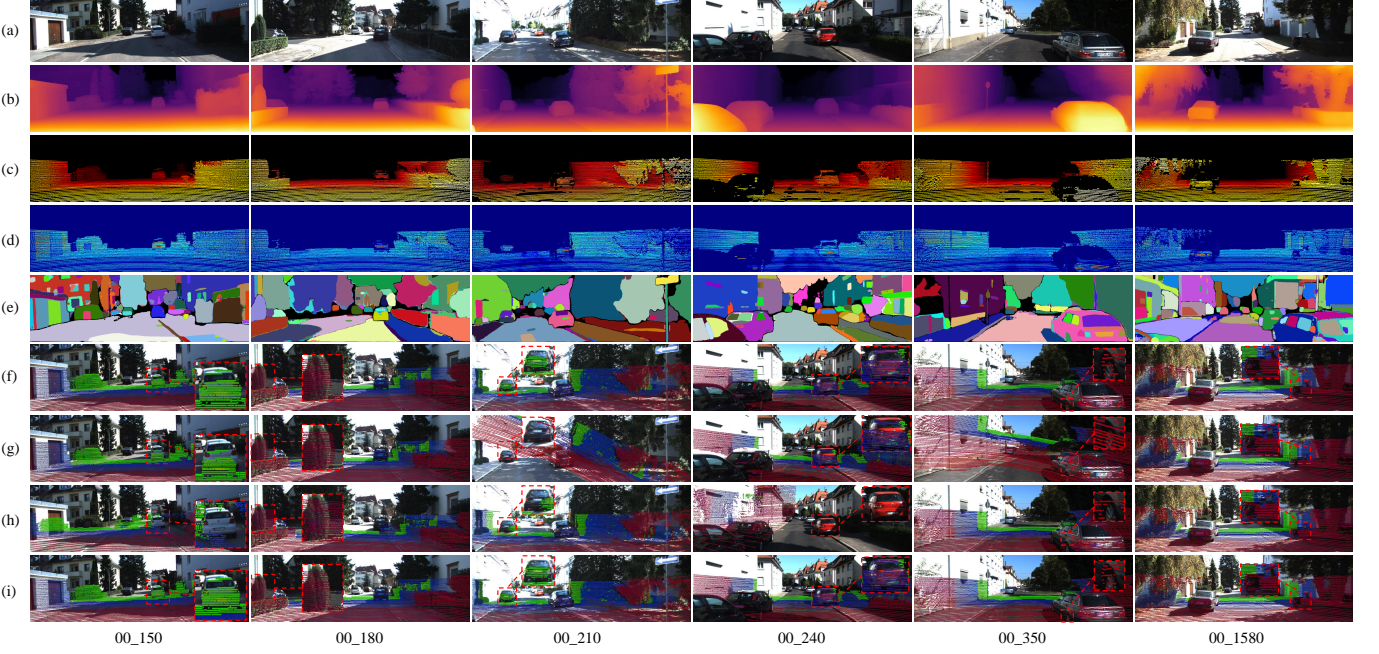


Fig. 6. Qualitative comparisons with SoTA target-free LCEC approaches on the KITTI odometry dataset: (a)-(e) RGB images, Depth images, LDP images, LIP images and image segmentation results; (f)-(i) experimental results achieved using ground truth, UMich, HKU-Mars and EdO-LCEC (ours), shown by merging LiDAR depth projections and RGB images, where significantly improved regions are shown with red dashed boxes.

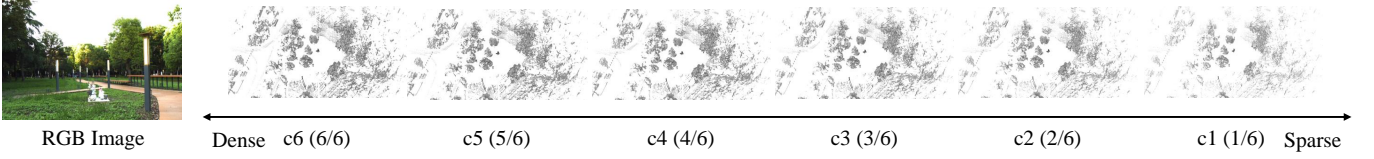


Fig. 7. We divided each point cloud into six equal parts and combined these segments to create point clouds with varying densities.

camera images. This impressive performance can be attributed to our proposed DPCM, a powerful cross-modal feature matching algorithm. DPCM utilizes structural and textural consistency to jointly constrain correspondences matching on both spatial and textural pathways. This largely increases reliable correspondences compared to DVL and MIAS-LCEC, thereby providing a more reliable foundation for extrinsic parameter optimization.

To evaluate the algorithm's adaptability to incomplete and sparse point clouds, we further segmented the already limited field-of-view point clouds from the MIAS-LCEC-TF360 dataset. Specifically, as shown in Fig. 7, we divide each point cloud into six equal parts based on the recorded temporal sequence of the points. By progressively combining these segments, we create point clouds with varying densities, ranging from 1/6 (c1) to the full 6/6 (c6) density. The calibration results presented in Fig. 8 show that EdO-LCEC achieves the smallest mean e_r and e_t , along with the narrowest interquartile range, compared to other approaches across different point cloud densities. This demonstrates the stability and adaptability of EdO-LCEC under challenging conditions involving sparse or incomplete point clouds.

C. Ablation Study and Analysis

To validate the contribution of structural consistency and

TABLE V
ABLATION STUDY OF STRUCTURAL AND TEXTURAL CONSISTENCY ON THE 00 SEQUENCE OF KITTI ODOMETRY. THE BEST RESULTS ARE SHOWN IN **BOLD** TYPE.

Consistency	Left Camera		Right Camera	
	Structural	Textural	e_r (°)	e_t (m)
✓	✓	✓	0.360	0.114
			0.340	0.102
	✓	✓	0.328	0.109
			0.476	0.185
✓	✓	✓	0.473	0.152
			0.435	0.146
✓	✓	✓	0.295	0.082
			0.336	0.118

textural consistency in DPCM, we conducted an ablation study comparing their individual and combined effects. As shown in Table V, both components significantly improve calibration accuracy. Specifically, structural consistency preserves local geometric features through mask-guided alignment, while textural consistency evaluates visual similarity around matched correspondences. Their combination enables DPCM to maintain robust matching performance even in challenging scenarios with sparse or occluded point clouds, which is a capability that existing methods (DVL and MIAS-LCEC) struggle to achieve. Additionally, MIAS-LCEC only compares the corner points within the matched segmented mask, while EdO-LCEC not only considers the corner points of the matched mask but also

TABLE VI

ABLATION STUDY OF MULTI-VIEW MULTI-SCENE JOINT OPTIMIZATION ON THE 00 SEQUENCE OF KITTI ODOMETRY. THE BEST RESULTS ARE SHOWN IN BOLD TYPE.

Components		Left Camera						Right Camera										
Multi-View	Multi-Scene	Magnitude	Rotation Error ($^{\circ}$)			Translation Error (m)			Magnitude	Rotation Error ($^{\circ}$)			Translation Error (m)					
Intensity	Depth	e_r ($^{\circ}$)	e_t (m)	Yaw	Pitch	Roll	X	Y	Z	e_r ($^{\circ}$)	e_t (m)	Yaw	Pitch	Roll	X	Y	Z	
✓		1.625	0.459	0.820	0.669	0.899	0.247	0.235	0.211	1.620	0.472	0.915	0.691	0.807	0.257	0.254	0.197	
✓	✓	1.387	0.358	0.755	0.579	0.711	0.189	0.208	0.153	1.641	0.459	1.012	0.679	0.738	0.257	0.257	0.178	
		✓	1.125	0.280	0.534	0.534	0.613	0.134	0.151	0.136	1.425	0.354	0.856	0.563	0.679	0.186	0.205	0.138
✓		✓	0.406	0.155	0.180	0.201	0.223	0.119	0.067	0.049	0.447	0.192	0.227	0.243	0.211	0.148	0.094	0.051
✓	✓	✓	0.339	0.110	0.179	0.167	0.162	0.069	0.063	0.039	0.480	0.138	0.322	0.239	0.150	0.096	0.084	0.033
✓	✓	✓	0.295	0.082	0.117	0.176	0.150	0.051	0.044	0.032	0.336	0.118	0.216	0.168	0.121	0.083	0.067	0.032

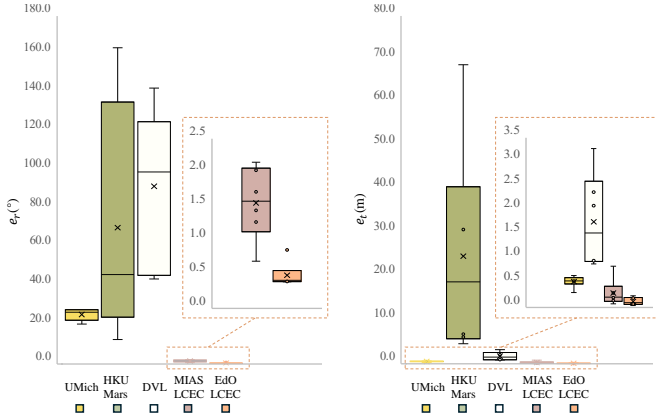


Fig. 8. Comparisons with SoTA approaches on the segmented point clouds from MIAS-LCEC-TF360. The zoomed-in region highlights the comparative details between the algorithms with higher accuracy. Since the results of CRLF are invalid, they were not included in the comparison.

includes those of other unmatched masks. This allows EdO-LCEC to achieve global attention when searching the potential available matches when LiDAR frames are sparse.

To explore the contribution of the generalizable scene discriminator as well as the multi-view and multi-scene joint optimization, we evaluate our algorithm’s performance with and without multi-view (including both textural and spatial perspective views) and multi-scene optimizations on the 00 sequence of KITTI odometry. The results presented in Table VI demonstrate that lacking any of these components significantly degrades calibration performance. In particular, calibration errors increase substantially when only single-view calibration is applied, as it lacks the comprehensive constraints provided by multi-view inputs. Additionally, the joint optimization from multiple scenes significantly improved the calibration accuracy compared to those only under multi-view optimization. These results confirm the advantage of incorporating spatial and textural constraints from multiple views and scenes, validating the robustness and adaptability of our environment-driven calibration strategy.

D. Comparison of Correspondence Matching

We present a comparison of correspondence matching results in Fig. 9. The visualized results indicate that our method significantly outperforms other correspondence matching algorithms employed in the comparison calibration methods.

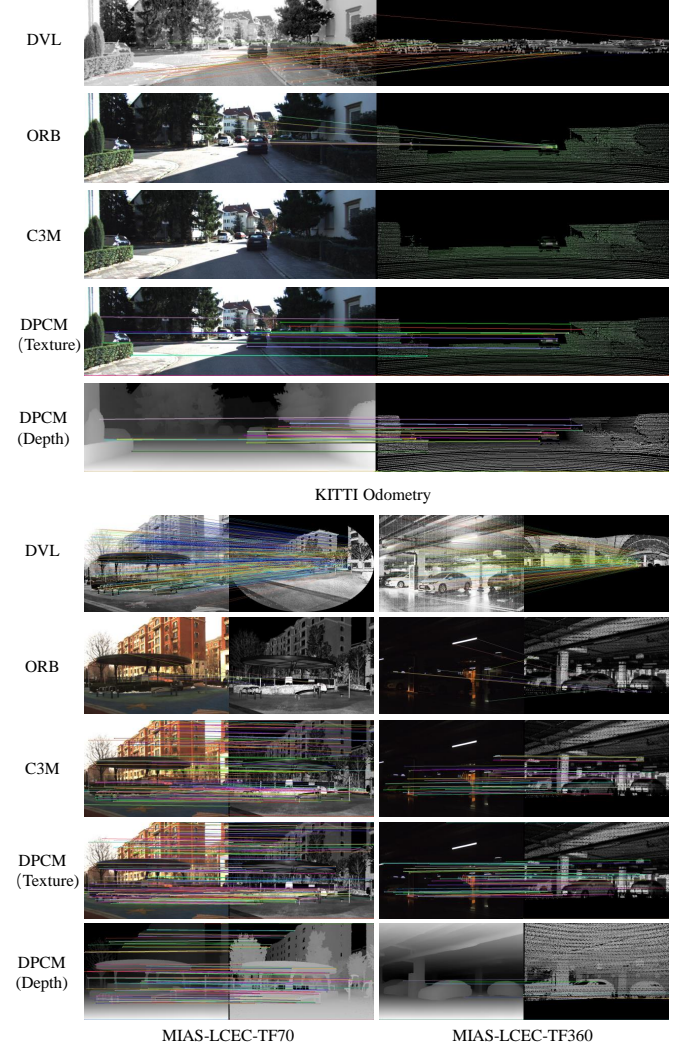


Fig. 9. Qualitative comparisons of correspondence matching.

Specifically, our approach yields substantially more correct correspondences than ORB, DVL (which employs SuperGlue for direct 3D-2D correspondence matching), and C3M (the cross-modal mask matching algorithm provided by MIAS-LCEC). This demonstrates the superior adaptability of DPCM, particularly in scenarios involving sparse point clouds with minimal geometric and textural information.

The ORB algorithm relies on the fast Harris corner detector for keypoint extraction and employs a binary descriptor for

efficient matching based on Hamming distance. While ORB performs well in image-to-image matching, it struggles with cross-modal feature matching, especially in LiDAR-camera integration scenarios. Conversely, while DVL and C3M perform adequately on dense point clouds such as those in the MIAS-LCEC-TF70, they face significant challenges when applied to the sparse point clouds in the KITTI odometry and MIAS-LCEC-TF360. The narrow overlapping field of view between LiDAR and camera in KITTI odometry creates difficulties in identifying reliable correspondences, particularly along the edges of the LiDAR field of view. This limitation significantly reduces the matching accuracy of DVL. Similarly, C3M, which restricts matching to corner points within aligned masks, struggles with sparse point clouds and limited sensor overlap.

Our proposed DPCM resolves these issues by incorporating both spatial and textural constraints. Unlike C3M, which treats mask instance matching as a strict constraint, DPCM uses it as a prior, enabling the generation of denser 3D-2D correspondences. This refinement significantly enhances the robustness of the algorithm in sparse environments and restricted fields of view, ensuring reliable calibration even under challenging conditions.

V. CONCLUSION

In this article, we explore extending a new definition called “environment-driven” for online LiDAR-camera extrinsic calibration. Unlike previous methods, our approach introduces environmental observation to maintain optimal performance across diverse and complex conditions. Specifically, we designed a scene discriminator that can automatically observe the calibration scene. This discriminator can guide cross-modal feature matching by evaluating the feature density through multi-modal features extracted by large vision models. By leveraging structural and textural consistency between LiDAR projections and camera images, our method achieves more reliable 3D-2D correspondence matching. Additionally, we modeled the calibration process as a multi-view and multi-scene joint optimization problem, achieving high-precision and robust extrinsic matrix estimation through multi-view optimization within individual scenes and joint optimization across multiple scenarios. Extensive experiments on real-world datasets demonstrate that our environment-driven calibration strategy achieves the state-of-the-art performance.

REFERENCES

- [1] J. Jiao *et al.*, “Lce-calib: automatic LiDAR-frame/event camera extrinsic calibration with a globally optimal solution,” *IEEE/ASME Transactions on Mechatronics*, vol. 28, no. 5, pp. 2988–2999, 2023.
- [2] R. Liu *et al.*, “Cost-effective mapping of mobile robot based on the fusion of uwb and short-range 2-D LiDAR,” *IEEE/ASME Transactions on Mechatronics*, vol. 27, no. 3, pp. 1321–1331, 2021.
- [3] Z. Zhang *et al.*, “Efficient motion planning based on kinodynamic model for quadruped robots following persons in confined spaces,” *IEEE/ASME Transactions on Mechatronics*, vol. 26, no. 4, pp. 1997–2006, 2021.
- [4] C. Pelau, D.-C. Dabija, and I. Ene, “What makes an AI device human-like? the role of interaction quality, empathy and perceived psychological anthropomorphic characteristics in the acceptance of artificial intelligence in the service industry,” *Computers in Human Behavior*, vol. 122, p. 106855, 2021.
- [5] Y. Tian, Y. Chang, F. H. Arias, C. Nieto-Granda, J. P. How, and L. Carlone, “Kimera-multi: Robust, distributed, dense metric-semantic slam for multi-robot systems,” *IEEE Transactions on Robotics*, vol. 38, no. 4, 2022.
- [6] Z. Huang *et al.*, “Online, target-free lidar-camera extrinsic calibration via cross-modal mask matching,” *IEEE Transactions on Intelligent Vehicles*, pp. 1–12, 2024.
- [7] J. Lin and F. Zhang, “R 3 live: A robust, real-time, rgb-colored, lidar-inertial-visual tightly-coupled state estimation and mapping package,” in *2022 International Conference on Robotics and Automation (ICRA)*. IEEE, 2022, pp. 10 672–10 678.
- [8] Y. Yu, P. Yun, B. Xue, J. Jiao, R. Fan, and M. Liu, “Accurate and robust visual localization system in large-scale appearance-changing environments,” *IEEE/ASME Transactions on Mechatronics*, vol. 27, no. 6, pp. 5222–5232, 2022.
- [9] C. R. Qi, W. Liu, C. Wu, H. Su, and L. J. Guibas, “Frustum pointnets for 3d object detection from rgb-d data,” in *Proceedings of the IEEE conference on computer vision and pattern recognition*, 2018, pp. 918–927.
- [10] J. Cui *et al.*, “ACSC: Automatic calibration for non-repetitive scanning solid-state LiDAR and camera systems,” *arXiv preprint arXiv:2011.08516*, 2020.
- [11] G. Yan *et al.*, “Joint camera intrinsic and LiDAR-camera extrinsic calibration,” in *2023 IEEE International Conference on Robotics and Automation (ICRA)*. IEEE, 2023, pp. 11 446–11 452.
- [12] J. Beltrán *et al.*, “Automatic extrinsic calibration method for LiDAR and camera sensor setups,” *IEEE Transactions on Intelligent Transportation Systems*, vol. 23, no. 10, pp. 17 677–17 689, 2022.
- [13] G. Koo *et al.*, “Analytic plane covariances construction for precise planarity-based extrinsic calibration of camera and LiDAR,” in *2020 IEEE International Conference on Robotics and Automation (ICRA)*. IEEE, 2020, pp. 6042–6048.
- [14] Y. Xie *et al.*, “A4LidarTag: Depth-based fiducial marker for extrinsic calibration of solid-state LiDAR and camera,” *IEEE Robotics and Automation Letters*, vol. 7, no. 3, pp. 6487–6494, 2022.
- [15] D. Tsai *et al.*, “Optimising the selection of samples for robust LiDAR camera calibration,” in *2021 IEEE International Intelligent Transportation Systems Conference (ITSC)*. IEEE, 2021, pp. 2631–2638.
- [16] C. Yuan *et al.*, “Pixel-level extrinsic self calibration of high resolution LiDAR and camera in targetless environments,” *IEEE Robotics and Automation Letters*, vol. 6, no. 4, pp. 7517–7524, 2021.
- [17] G. Pandey *et al.*, “Automatic extrinsic calibration of vision and LiDAR by maximizing mutual information,” *Journal of Field Robotics*, vol. 32, no. 5, pp. 696–722, 2015.
- [18] Y. Wang *et al.*, “Automatic registration of point cloud and panoramic images in urban scenes based on pole matching,” *International Journal of Applied Earth Observation and Geoinformation*, vol. 115, p. 103083, 2022.
- [19] Y. Han *et al.*, “Auto-calibration method using stop signs for urban autonomous driving applications,” in *2021 IEEE International Conference on Robotics and Automation (ICRA)*. IEEE, 2021, pp. 13 179–13 185.
- [20] Y. Liao *et al.*, “SE-Calib: Semantic edges based LiDAR-camera bore-sight online calibration in urban scenes,” *IEEE Transactions on Geoscience and Remote Sensing*, 2023, DOI: 10.1109/TGRS.2023.3278024.
- [21] J. Borer *et al.*, “From chaos to calibration: A geometric mutual information approach to target-free camera LiDAR extrinsic calibration,” in *Proceedings of the IEEE/CVF Winter Conference on Applications of Computer Vision (WACV)*, 2024, pp. 8409–8418.
- [22] X. Lv *et al.*, “LCCNet: LiDAR and camera self-calibration using cost volume network,” in *Proceedings of the IEEE/CVF Conference on Computer Vision and Pattern Recognition (CVPR)*, 2021, pp. 2894–2901.
- [23] J. Shi *et al.*, “CalibRCNN: Calibrating camera and LiDAR by recurrent convolutional neural network and geometric constraints,” in *2020 IEEE/RSJ International Conference on Intelligent Robots and Systems (IROS)*. IEEE, 2020, pp. 10 197–10 202.
- [24] G. Zhao *et al.*, “CalibDNN: multimodal sensor calibration for perception using deep neural networks,” in *Signal Processing, Sensor/Information Fusion, and Target Recognition XXX*, vol. 11756. SPIE, 2021, pp. 324–335.
- [25] G. Iyer *et al.*, “CalibNet: Geometrically supervised extrinsic calibration using 3D spatial transformer networks,” in *2018 IEEE/RSJ International Conference on Intelligent Robots and Systems (IROS)*. IEEE, 2018, pp. 1110–1117.
- [26] K. Yuan *et al.*, “RGGNet: Tolerance aware LiDAR-camera online calibration with geometric deep learning and generative model,” *IEEE Robotics and Automation Letters*, vol. 5, no. 4, pp. 6956–6963, 2020.

- [27] A. Geiger *et al.*, “Are we ready for autonomous driving? the KITTI vision benchmark suite,” in *2012 IEEE conference on Computer Vision and Pattern Recognition (CVPR)*. IEEE, 2012, pp. 3354–3361.
- [28] C. Zhang *et al.*, “Faster Segment Anything: Towards lightweight sam for mobile applications,” *arXiv preprint arXiv:2306.14289*, 2023.
- [29] K. Koide *et al.*, “General, single-shot, target-less, and automatic LiDAR-camera extrinsic calibration toolbox,” in *2023 IEEE International Conference on Robotics and Automation (ICRA)*, 2023, pp. 11 301–11 307.
- [30] N. Ou *et al.*, “Targetless extrinsic calibration of camera and low-resolution 3D LiDAR,” *IEEE Sensors Journal*, 2023.
- [31] F. Lv and K. Ren, “Automatic registration of airborne LiDAR point cloud data and optical imagery depth map based on line and points features,” *Infrared Physics & Technology*, vol. 71, pp. 457–463, 2015.
- [32] J. Castorena *et al.*, “Autocalibration of LiDAR and optical cameras via edge alignment,” in *2016 IEEE International Conference on Acoustics, Speech and Signal Processing (ICASSP)*. IEEE, 2016, pp. 2862–2866.
- [33] S. Tang *et al.*, “Robust calibration of vehicle solid-state LiDAR-camera perception system using line-weighted correspondences in natural environments,” *IEEE Transactions on Intelligent Transportation Systems*, 2023, DOI: 10.1109/TITS.2023.3328062.
- [34] D. Zhang *et al.*, “An overlap-free calibration method for LiDAR-camera platforms based on environmental perception,” *IEEE Transactions on Instrumentation and Measurement*, vol. 72, pp. 1–7, 2023.
- [35] J. Yin *et al.*, “Automatic and targetless LiDAR-camera extrinsic calibration using edge alignment,” *IEEE Sensors Journal*, 2023.
- [36] N. Ou *et al.*, “Targetless LiDAR-camera calibration via cross-modality structure consistency,” *IEEE Transactions on Intelligent Vehicles*, 2023, DOI: 10.1109/TIV.2023.3337490.
- [37] J. Li *et al.*, “Automatic registration of panoramic image sequence and mobile laser scanning data using semantic features,” *ISPRS Journal of Photogrammetry and Remote Sensing*, vol. 136, pp. 41–57, 2018.
- [38] T. Ma *et al.*, “CRLF: Automatic calibration and refinement based on line feature for LiDAR and camera in road scenes,” *arXiv preprint arXiv:2103.04558*, 2021.
- [39] Y. Zhu *et al.*, “Online camera-LiDAR calibration with sensor semantic information,” in *2020 IEEE International Conference on Robotics and Automation (ICRA)*. IEEE, 2020, pp. 4970–4976.
- [40] P.-E. Sarlin *et al.*, “SuperGlue: Learning feature matching with graph neural networks,” in *Proceedings of the IEEE/CVF Conference on Computer Vision and Pattern Recognition (CVPR)*, 2020, pp. 4938–4947.
- [41] L. Yang *et al.*, “Depth Anything V2,” *arXiv:2406.09414*, 2024.
- [42] Kirillov *et al.*, “Segment Anything,” in *Proceedings of the IEEE/CVF International Conference on Computer Vision (CVPR)*, 2023, pp. 4015–4026.
- [43] N. Schneider *et al.*, “RegNet: Multimodal sensor registration using deep neural networks,” in *2017 IEEE Intelligent Vehicles Symposium (IV)*. IEEE, 2017, pp. 1803–1810.

Environment-Driven Online LiDAR-Camera Extrinsic Calibration

Supplementary Material

VI. DETAILS OF THE ALGORITHM IMPLEMENTATION

As presented in the ‘‘Dual-Path Correspondence Matching’’ in Sect. III-B, we initially adopted the method described in [6] for cross-modal mask matching. [6] proved that when two 3D LiDAR points \mathbf{q}^V (reference) and \mathbf{p}^V (target) in the virtual camera coordinate system are close in depth, the relationship of their projection coordinates $\tilde{\mathbf{p}}_{v,c}$ on virtual image and camera image can be written by follows:

$$\tilde{\mathbf{p}}_c \approx A\tilde{\mathbf{p}}_v + \mathbf{b}. \quad (12)$$

In practice, we use the following affine transformation:

$$(\tilde{\mathbf{p}}_c \quad \tilde{\mathbf{q}}_c) = \begin{pmatrix} s\mathbf{R}^A & \mathbf{t}^A \\ \mathbf{0}^\top & 1 \end{pmatrix} (\tilde{\mathbf{p}}_v \quad \tilde{\mathbf{q}}_v) \quad (13)$$

to represent this affine transformation (mentioned in Sect. III-B), where $\mathbf{R}^A \in SO(2)$ represents the rotation matrix, \mathbf{t}^A denotes the translation vector, and s represents the scaling factor. We can assume that after the affine transformation, any points within a given mask in the LIP image perfectly align with the corresponding points from the RGB image, and thus:

$$\begin{aligned} \hat{\mathbf{c}}^V &= s\mathbf{R}^A \mathbf{c}^V + \mathbf{t}^A, \\ \hat{\mathbf{o}}^V &= s\mathbf{R}^A \mathbf{o}^V + \mathbf{t}^A. \end{aligned} \quad (14)$$

where $\hat{\mathbf{o}}^V$ and $\hat{\mathbf{c}}^V$ represent the updated coordinates of the instance’s center and corner points in the virtual image, respectively. In this case, \mathbf{R}^A can be obtained using the following expression:

$$\mathbf{R}^A = \begin{pmatrix} \cos \theta & -\sin \theta \\ \sin \theta & \cos \theta \end{pmatrix}, \quad (15)$$

where

$$\theta = \frac{1}{N} \sum_{i=1}^N \left(\arctan \frac{\mathbf{1}_y^\top (\mathbf{c}_i^V - \mathbf{o}^V)}{\mathbf{1}_x^\top (\mathbf{c}_i^V - \mathbf{o}^V)} - \arctan \frac{\mathbf{1}_y^\top (\mathbf{c}_i^C - \mathbf{o}^C)}{\mathbf{1}_x^\top (\mathbf{c}_i^C - \mathbf{o}^C)} \right) \quad (16)$$

is the angle between the vectors originating from the mask centers and pointing to their respective matched corner points. s can then be expressed as follows:

$$s = \frac{w^C h^C}{w^V h^V}, \quad (17)$$

which represents the ratio between the areas of the bounding boxes associated with the RGB image and the LIP image. Finally, according to (14), \mathbf{t}^A can be obtained as follows:

$$\mathbf{t}^A = \mathbf{o}^C - s\mathbf{R}^A \mathbf{o}^V. \quad (18)$$

In DPCM, we utilize the affine transformation estimated by (15)-(18) as a semantic prior to guide the dense correspondence matching between LiDAR and camera.

Additionally, the component $H(\mathbf{e}_{i,k}^V, \mathbf{e}_{j,k}^C)$ of the structural consistency mentioned in Sect. III-B is defined as follows:

$$H(\mathbf{e}_{i,k}^V, \mathbf{e}_{j,k}^C) = \frac{\|(\mathbf{e}_{i,k}^V - \hat{\mathbf{c}}_i^V) - (\mathbf{e}_{j,k}^C - \mathbf{c}_j^C)\|_2}{\|\mathbf{e}_{i,k}^V - \hat{\mathbf{c}}_i^V\|_2 + \|\mathbf{e}_{j,k}^C - \mathbf{c}_j^C\|_2}, \quad (19)$$

which represents the similarity of the neighboring vertices between the current and target corner points.

For the spatial-temporal relative pose optimization, as presented in Sect. III-C, we utilize a Gaussian kernel $\mathcal{K}(d'_j, \bar{d}')$ to calculate the depth-normalized reprojection error. In detail, $\mathcal{K}(d'_j, \bar{d}')$ is defined as follows:

$$\mathcal{K}(d'_j, \bar{d}') = \exp \left(-\frac{\|d'_j - \bar{d}'\|^2}{2\bar{d}'^2} \right), \quad (20)$$

where \bar{d}' is the true average depth of the correspondences.

In our algorithm implementation, we use the pinhole model as the projection model to calculate the reprojection error presented in (7) and (10). When the camera intrinsic matrix \mathbf{K} is known, the 3D LiDAR point $\mathbf{p}^L = [x^L, y^L, z^L]^\top$ can be projected onto a 2D image pixel $\mathbf{p} = [u, v]^\top$ using the following expression:

$$\pi(\mathbf{p}^L) = \tilde{\mathbf{p}} = \frac{\mathbf{K}\mathbf{p}^L}{(\mathbf{p}^L)^\top \mathbf{1}_z}, \quad (21)$$

where $\tilde{\mathbf{p}}$ represents the homogeneous coordinates of \mathbf{p} and $\mathbf{1}_z = [0, 0, 1]^\top$. Given the extrinsic transformation ${}_L^C \mathbf{T}$, the reprojection between the correspondence $(\mathbf{p}_i^L, \mathbf{p}_i)$ can be obtained as follows:

$$\epsilon_i = \|\pi({}_L^C \mathbf{T} \mathbf{p}_i^L) - \tilde{\mathbf{p}}_i\|_2 = \left\| \frac{\mathbf{K}({}_L^C \mathbf{R} \mathbf{p}_i^L + {}_L^C \mathbf{t})}{({}_L^C \mathbf{R} \mathbf{p}_i^L + {}_L^C \mathbf{t})^\top \mathbf{1}_z} - \tilde{\mathbf{p}}_i \right\|_2. \quad (22)$$

By applying the Gaussian normalization G given in (8), the reprojection errors of different correspondences are provided with weights based on the depth distribution.

VII. CALIBRATION PARAMETERS

To foster future research toward LiDAR-camera sensor fusion, we release the calibration parameters that we obtained with our method for the 00 sequence of the KITTI odometry. In detail, we provide the rotation matrices and translation vectors for projecting the LiDAR point cloud into the camera image or rendering LiDAR point clouds with colors.

Calibration Parameters for Left RGB Camera

$$\begin{aligned} \mathbf{R} &= \begin{bmatrix} -2.5805e-04 & -9.9997e-01 & -7.5245e-03 \\ -6.8854e-03 & 7.5261e-03 & -9.9995e-01 \\ 9.9998e-01 & -2.0623e-04 & -6.8872e-03 \end{bmatrix} \\ \mathbf{t} &= [0.070478 \quad -0.057913 \quad -0.286353]^\top \end{aligned}$$

Calibration Parameters for Right RGB Camera

$$\begin{aligned} \mathbf{R} &= \begin{bmatrix} -5.3850e-04 & -9.9998e-01 & -6.6623e-03 \\ -8.1213e-03 & 6.6665e-03 & -9.9994e-01 \\ 9.9997e-01 & -4.8437e-04 & -8.1247e-03 \end{bmatrix} \\ \mathbf{t} &= [-0.494557 \quad -0.042731 \quad -0.261487]^\top \end{aligned}$$

An example of the data fusion result using our extrinsic calibration parameters for the left camera in KITTI odometry is shown in Fig. 10.



Fig. 10. An example of the data fusion result on KITTI odometry using our calibration parameters.

TABLE VII
DETAILS OF COMPARISON METHODS.

Methods	Publication	Type	Parameterization or Basic Tools	Computation Speed	Accuracy	Provide Code?
UMich [17]	JFR 2015	MI-based	Mutual Information	Medium	Medium	Yes
RegNet [43]	IV 2017	Learning-based	CNN	Medium	Medium	No
CalibNet [25]	IROS 2018	Learning-based	Geometrically Supervised Deep Learning Network	High	Low	Yes
RGGNet [26]	RAL 2020	Learning-based	Deep Learning Network, Riemannian Geometry	High	Medium	Yes
CalibRCNN [23]	IROS 2020	Learning-based	RCNN	Medium	Medium	No
CalibDNN [24]	SPIE 2021	Learning-based	Deep Learning Network	Medium	Medium	No
LCCNet [22]	CVPR 2021	Learning-based	CNN, L1-Loss	High	Medium	Yes
HKU-Mars [16]	RAL 2021	Edge-based	Adaptive Voxel	Low	Very Low	Yes
CRLF [38]	arXiv 2021	Semantic-based	Segmented Road Pole and Lane, Perspective-3-Lines	Low	Low	Yes
DVL [29]	ICRA 2023	Point-based	SuperGlue, RANSAC, Normalized Information Distance	Medium	High	Yes
Borer <i>et al.</i> [21]	WACV 2024	MI-based	Geometric Mutual Information	High	High	No
MIAS-LCEC [6]	T-IV 2024	Semantic-based	MobileSAM, C3M, PnP	Low	High	Yes

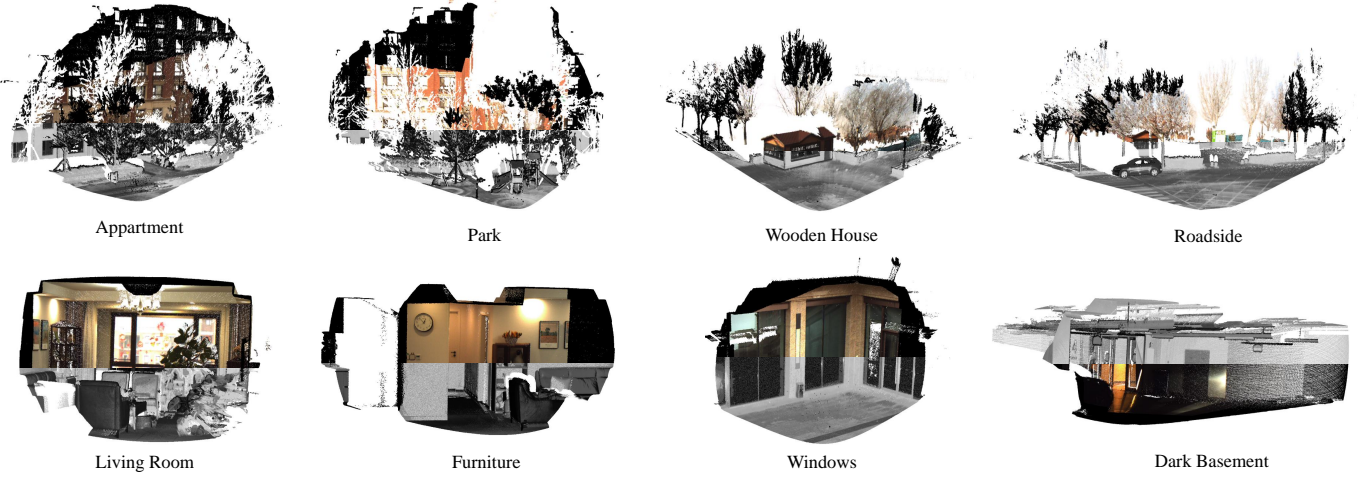


Fig. 11. Visualization of EdO-LCEC calibration results through LiDAR and camera data fusion on MIAS-LCEC datasets.

TABLE VIII
DATASET STATISTICS OF KITTI ODOMETRY 00-09 SEQUENCES.

	00	01	02	03	04	05	06	07	08	09
Initial Pairs	4541	1101	4661	801	271	2761	1101	1101	4071	4091
Downsampling	10	10	10	10	2	10	10	10	10	410
Evaluated Pairs	455	111	467	81	136	277	111	111	408	410

VIII. DETAILS OF EXPERIMENTAL CONFIGURATION

A. Datasets

We have conducted extensive experiments on KITTI odometry and MIAS-LCEC (including MIAS-LCEC-TF70 and MIAS-LCEC-TF360) datasets. Now we provide their details:

- **KITTI odometry:** KITTI odometry is a large-scale public dataset recorded using a vehicle equipped with two RGB

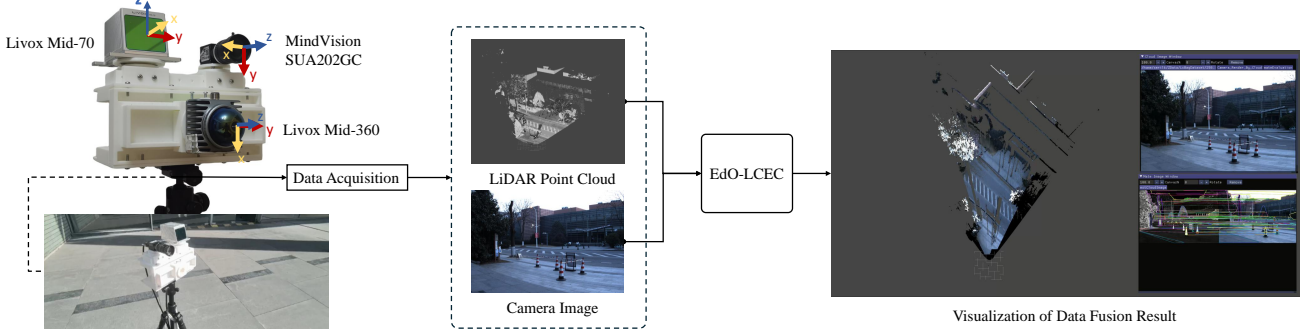


Fig. 12. Data preparation pipeline using our sensor setup.

cameras Point Grey Flea 2 and one LiDAR of type Velodyne HDL-64E. Sensor data is captured at 10 Hz. We utilize the first 10 sequences (00-09) for evaluation.

- **MIAS-LCEC-TF70:** MIAS-LCEC-TF70 is a diverse and challenging dataset that contains 60 pairs of 4D point clouds (including spatial coordinates with intensity data) and RGB images, collected using a Livox Mid-70 LiDAR and a MindVision SUA202GC camera, from a variety of indoor and outdoor environments, under various scenarios as well as different weather and illumination conditions. This dataset is divided into six subsets: residential community, urban freeway, building, challenging weather, indoor, and challenging illumination, to comprehensively evaluate the algorithm performance.
- **MIAS-LCEC-TF360:** MIAS-LCEC-TF360 contains 12 pairs of 4D point clouds and RGB images, collected using a Livox Mid-360 LiDAR and a MindVision SUA202GC camera from both indoor and outdoor environments. Since the Livox Mid-360 LiDAR has a scanning range of 360°, it produces a sparser point cloud compared to that generated by the Livox Mid-70 LiDAR. Additionally, the significant difference in the FoV between this type of LiDAR and the camera results in only a small overlap in the collected data. Consequently, this dataset is particularly well-suited for evaluating the adaptability of algorithms to challenging scenarios.

B. Data Preparation

The dataset statistics of KITTI odometry are presented in Table VII. It can be observed that there are a total of 24500 pairs of point clouds and images in KITTI odometry. Note that most of the SoTA comparison methods are slow to complete calibration with a single frame. For the comparison algorithms that provided source code, we performed calibration every ten frames (except for 2 frames in 04 sequence), enhancing the efficiency of the experiments without compromising the validity of the evaluation.

The data preparation pipeline for our MIAS-LCEC datasets is illustrated in Fig. 12. Our experimental platform integrates two DJI Livox solid-state LiDARs (Mid-70 and Mid-360) and a MindVision MV-SUA202GC global-shutter CMOS camera for synchronized cross-modal data acquisition. Both LiDARs

operate at 200,000 points/s. However, the Mid-70 captures dual returns while the Mid-360 records only the first return. For each scene, we accumulate 15-20 seconds of LiDAR scans to ensure dense point cloud coverage, paired with RGB images at 1,200×800 pixel resolution captured by the camera, whose intrinsic parameters were pre-calibrated offline and remained fixed throughout all experiments.

C. Details of Comparison Methods

The details of the comparison methods are illustrated in Table VII. For algorithms that did not release their code, we directly reference the results published in their papers. Notably, RegNet [43], Borer *et al.* [21], and CalibDNN [24] employ different experimental datasets and evaluation processes, which limits the potential for a fully quantitative comparison. Furthermore, these methods do not specify which frames from the KITTI dataset were used for training and testing. Therefore, we rely on the published results to compare these approaches to others on the KITTI odometry 00 sequence.

IX. MORE VISUALIZATION RESULTS

In this section, we provide more detailed visualization results of EdO-LCEC through LiDAR and camera data fusion on MIAS-LCEC datasets. Fig. 11 demonstrates that the LiDAR point cloud and camera image aligned almost perfectly along the textural and geometric edges, proving the accuracy of our calibration results. It can also be observed that our method performs well in challenging conditions, particularly under poor illumination and adverse weather, or when few geometric features are detectable. This impressive data fusion result further validates the critical role of LiDAR-camera extrinsic calibration. The seamless integration of spatial and textural modalities equips robots with a human-like perceptual ability to interpret and interact with their surroundings. Our environment-driven approach bridges the gap toward the flexible and adaptive machines often envisioned in science fiction.